

RESEARCH ARTICLE

10.1002/2014JC010504

Dynamics of the surface layer diurnal cycle in the equatorial Atlantic Ocean (0°, 23°W)

Jacob O. Wenegrat¹ and Michael J. McPhaden^{1,2}¹School of Oceanography, University of Washington, Seattle, Washington, USA, ²Pacific Marine Environmental Laboratory, National Oceanic and Atmospheric Administration, Seattle, Washington, USA

Key Points:

- Direct observations of the near-surface diurnal cycle in the equatorial Atlantic
- Diurnal shear layers are regularly observed during steady trade wind conditions
- Marginal instability of the EUC suggests deep-cycle turbulence in the Atlantic

Correspondence to:

J. O. Wenegrat,
wenegrat@uw.edu

Citation:

Wenegrat, J. O., and M. J. McPhaden (2015), Dynamics of the surface layer diurnal cycle in the equatorial Atlantic Ocean (0°, 23°W), *J. Geophys. Res. Oceans*, 120, doi:10.1002/2014JC010504.

Received 13 OCT 2014

Accepted 23 DEC 2014

Accepted article online 30 DEC 2014

Abstract A 15 year time series (1999–2014) from the 0°, 23°W Prediction and Research Moored Array in the Tropical Atlantic (PIRATA) mooring, which includes an 8 month record (October 2008 to June 2009) of high-resolution near-surface velocity data, is used to analyze the diurnal variability of sea surface temperature, shear, and stratification in the central equatorial Atlantic. The ocean diurnal cycle exhibits pronounced seasonality that is linked to seasonal variations in the surface wind field. In boreal summer and fall, steady trade winds and clear skies dominate, with limited diurnal variability in sea surface temperature. Diurnal shear layers, with reduced Richardson numbers, are regularly observed descending into the marginally unstable equatorial undercurrent below the mixed layer, conditions favorable for the generation of deep-cycle turbulence. In contrast, in boreal winter and spring, winds are lighter and more variable, mixed layers are shallow, and diurnal variability of sea surface temperature is large. During these conditions, diurnal shear layers are less prominent, and the stability of the undercurrent increases, suggesting seasonal covariance between diurnal near-surface shear and deep-cycle turbulence. Modulation of the ocean diurnal cycle by tropical instability waves is also identified. This work provides the first observational assessment of the diurnal cycle of near-surface shear, stratification, and marginal instability in the equatorial Atlantic, confirming previous modeling results and offering a complementary perspective on similar work in the equatorial Pacific.

1. Introduction

The daily cycle of solar insolation is one of the most fundamental drivers of variability in the Earth system, with prominent effects on both the atmosphere and oceans. The diurnal cycle of heat flux between the surface ocean and the atmosphere results in a concomitant cycle of sea surface temperature (SST), which was observed as early as 1854 by William Henry Smyth, who recorded 3–4°C diurnal variations in Mediterranean SST [Smyth, 1854]. Around the same time, the importance of these diurnal SST variations for ocean variability and air-sea interaction was posited by Matthew Fontaine Maury who vividly described the diurnal variability of atmosphere and oceans as “cogs, and ratchets, and wheels in that grand and exquisite machinery which governs the sea” [Maury, 1855].

Subsequent to those early observations, it was established that much of the global ocean exhibits significant diurnal variability of SST [Stommel *et al.*, 1969; Halpern and Reed, 1976; Stuart-Menteth *et al.*, 2003], with the largest annual mean diurnal SST ranges reaching 0.5–1°C in the tropics [Bernie *et al.*, 2007]. The diurnal cycle of SST has also been shown to feedback to the atmosphere in a variety of important ways [Clayson and Curry, 1996], including modifying the heat and moisture content in the atmospheric boundary layer, with significant effects on the lifecycle of convective cloud systems and associated precipitation [Chen and Houze, 1997; Clayson and Chen, 2002; Dai and Trenberth, 2004; Woolnough *et al.*, 2007]. Modeling studies also reveal that diurnal variability modifies SST on intraseasonal, seasonal, and longer time scales [Shinoda, 2005; Danabasoglu *et al.*, 2006; Bernie *et al.*, 2007, 2008], which presents a challenge for accurate climate modeling [Flato *et al.*, 2013; Sillmann *et al.*, 2013].

The diurnal cycle of solar heating also has important dynamic effects, as afternoon stratification of the near-surface layer inhibits the vertical transfer of momentum that is input at the ocean surface by the wind [Price *et al.*, 1986]. Over the course of the day, the trapping of momentum can lead to the creation of a highly sheared near-surface diurnal jet. After the midday peak of solar insolation, this sheared diurnal jet can decrease the near-surface Richardson number, moving the flow toward shear instability [Price *et al.*, 1986;

Cronin and Kessler, 2009; Smyth et al., 2013). Recent work in the tropical Pacific suggests that the descent of this low Richardson number shear layer into a marginally unstable equatorial undercurrent system can provide the initiation mechanism for deep-cycle turbulence [*Smyth et al., 2013; Pham et al., 2013*], leading to large vertical fluxes of heat and momentum through the thermocline [*Lien et al., 1995; Moum et al., 2013*].

While the fundamental role that the diurnal cycle of near-surface stratification, and shear, plays in the dynamics of the equatorial Pacific has been extensively documented [*Gregg et al., 1985; Moum and Caldwell, 1985; Peters et al., 1994; Sun et al., 1998*], to date the diurnal cycle in the equatorial Atlantic has not been as fully characterized. Recent microstructure field campaigns have provided an initial view into the turbulent processes occurring in the upper equatorial Atlantic, with suggestions of deep-cycle turbulence, although reduced in strength relative to the Pacific [*Crawford and Osborn, 1979; Hummels, 2012; Hummels et al., 2013, 2014*]. The diurnal cycle of turbulence has not been as clearly identified in observations, although this may result from limited temporal resolution, as modeling studies suggest an expectation of processes similar to those identified in the Pacific [*Skielka et al., 2011; Wade et al., 2011*].

Here we utilize a long time series spanning 15 years of atmosphere and ocean data from the 0°, 23°W PIRATA mooring in the central equatorial Atlantic (Figure 1) [*Servain et al., 1998; Boulès et al., 2008*] to address the dynamics of the surface layer diurnal cycle. This mooring is located in the Atlantic cold tongue region (Figure 1), enabling comparisons with the extensive diurnal cycle literature from 0°, 140°W in the Pacific [*Gregg et al., 1985; Moum and Caldwell, 1985; Bond and McPhaden, 1995; Lien et al., 1995; Sun et al., 1998; Smyth et al., 2013*]. Additionally, this time series is augmented with data from an 8 month enhanced monitoring period (EMP) where high-resolution velocity observations resolved hourly horizontal currents between depths of 3.75 and 150 m.

Together these observations, which are described in section 2, enable a unique description of diurnal variability spanning from the ocean surface to the thermocline. Section 3 begins with a description of the seasonal cycle of diurnal SST in relation to atmospheric forcing, followed in section 4 by a detailed examination of the mixed-layer processes which mediate the surface response to forcing. Finally, section 5 examines the seasonal cycle of stability of the undercurrent layer below the mixed layer, a proxy for deep-cycle turbulence [*Smyth and Moum, 2013*]. To the best of our knowledge, this represents the first in situ observational assessment of the diurnal cycle of near-surface shear, stratification, and marginal instability in the equatorial Atlantic Ocean.

2. Data

2.1. PIRATA Data

PIRATA moorings are instrumented with a suite of subsurface temperature and salinity measurements (Table 1). In addition to the subsurface measurements, the 0°, 23°W mooring collects enhanced atmospheric measurements as part of the OceanSITES program of deep water flux measurement sites (<http://www.pmel.noaa.gov/tao/oceansites/>). Included in the surface instrumentation are measurements of wind speed and direction, air temperature, relative humidity, rainfall, and downwelling shortwave and longwave radiation. Daily averaged observations are transmitted from the mooring via real-time telemetry, with 1–10 min resolution data available on recovery of the mooring. Surface and subsurface observations utilized in this study are summarized in Table 1.

The uppermost temperature observation is at 1 m depth. Significant temperature gradients can develop in the upper few meters of the water column, particularly during conditions of low wind stress [*Donlon et al., 2002; Ward, 2006*]. Thus, while we will reference the 1 m observations as being representative of a bulk SST, they do not necessarily represent the skin temperature directly associated with atmosphere-ocean heat flux.

Surface flux, and wind stress, values are calculated from mooring data using the COARE 3b bulk algorithm [*Fairall et al., 2003*].

2.2. Enhanced Monitoring Period Data

During an Enhanced Monitoring Period (EMP) from 13 October 2008 to 17 June 2009, the mooring was instrumented with a 600 kHz acoustic Doppler current profiler (ADCP), deployed in a downward-facing position on the mooring bridle, returning horizontal velocities between 3.75 and 35 m depth in 0.75 m vertical

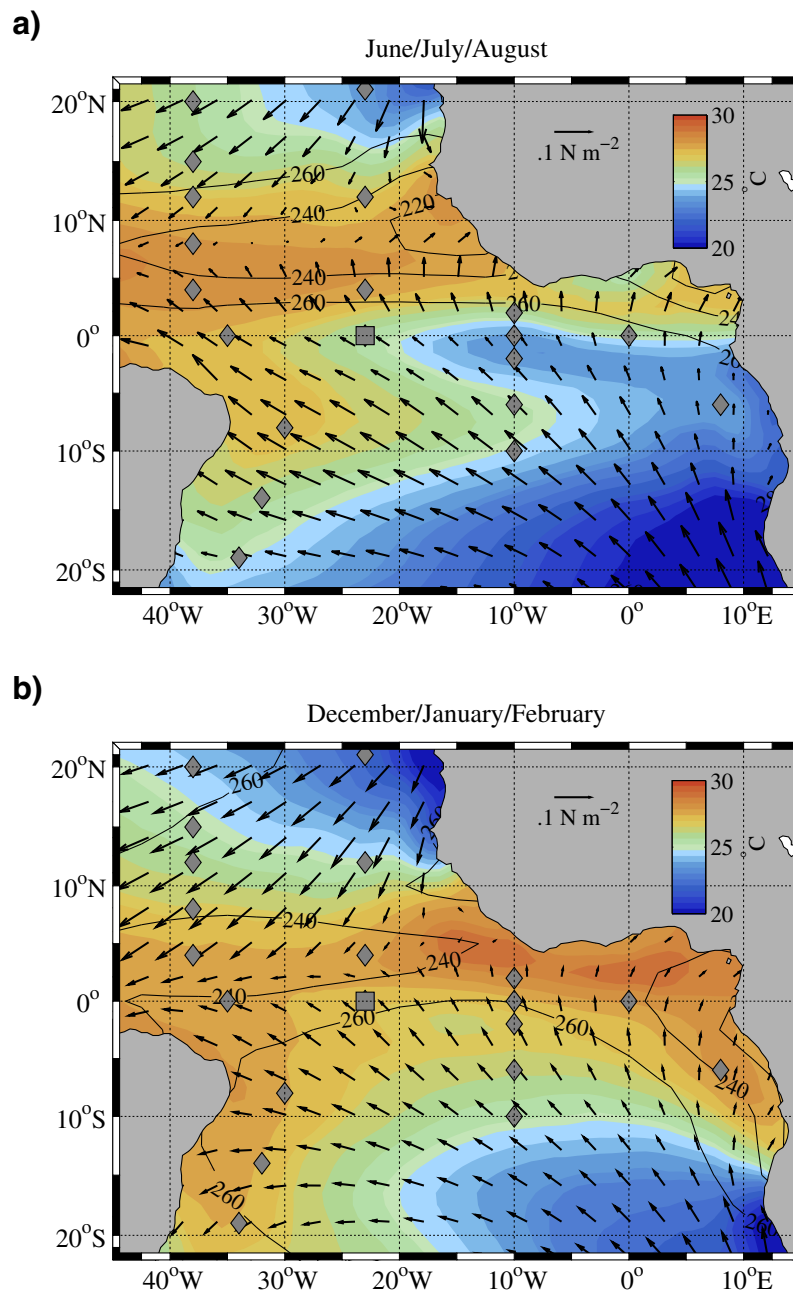


Figure 1. Location of the Prediction and Research Moored Array in the Tropical Atlantic moorings (gray diamonds; study location, gray square), with seasonal average variables for (a) boreal summer (June, July, and August) and (b) boreal winter (December, January, and February). Color scale: sea surface temperature (SST) from 1999 to 2014 from NOAA optimally interpolated SST version 2 [Reynolds *et al.*, 2002]. Vectors: wind stress from 1999 to 2009 from the scatterometer climatology of ocean winds [Risien and Chelton, 2008], with scale shown on plot. Contours: NOAA interpolated top of atmosphere outgoing longwave radiation (OLR; values shown on contours in units of Wm^{-2}) from 1999 to 2014 [Liebmann and Smith, 1996].

however, additional temperature observations were available, including observations at 13 m (Table 1). The 1 m salinity sensor returned data for only the first 22 days of the record, and the 5 m observations were flagged while being quality controlled and are excluded from this analysis. Near-surface salinity exhibits limited diurnal variability at this location ($\sim \pm 0.01$ psu) [Drushka *et al.*, 2014], and correlation between the available 1 and 20 m salinity observations was high ($r = 0.93$). Hence, we fill the missing salinity observations through linear regression using the 20 m values. Our results are not sensitive to this choice, and a variety of

bins. Hourly means were formed from ensemble averages of 120 1 Hz consecutive samples at the top of the hour in order to limit the effect of mooring motion due to surface waves. Several of the near-surface ADCP bins were biased by sidelobe reflection off instruments on the mooring line. Corrupted bins were identified by visual inspection of echo intensity and vertical profiles of velocity and were removed from subsequent analysis. ADCP velocity measurements were validated against point current meter observations at several depths, with typical correlation coefficients greater than $r = 0.98$, and root-mean-square differences less than 3.5 cm s^{-1} (see Wenegrat *et al.* [2014] for additional discussion of ADCP data). An additional upward-facing 150 kHz ADCP was deployed approximately 12.5 km west of the surface mooring, measuring hourly horizontal currents in 8 m vertical bins which were then mapped to a uniform 5 m grid between 150 and 35 m.

During the EMP, the 10 m temperature sensor did not return data;

Table 1. Summary of 0°, 23°W Data

Observation	Height (m)	Sampling Frequency
<i>Surface Observations</i>		
Wind speed/direction	4	10 minute
SWR	3.5	2 minute
LWR	3.5	2 minute
Rain	3.5	10 minute
Air temperature	3	10 minute
Relative humidity	3	10 minute
Observation	Depth (m)	Sampling Frequency
<i>Subsurface Observations</i>		
Temperature	1, 5, 10 ^a , 13 ^b , 20, 23 ^b , 40, 60, 80, 100, 120	10 minute
Salinity	1 ^a , 5 ^a , 20, 40, 60, 80, 100, 120	10 minute
600 kHz ADCP ^b	3.75–35 (0.75 m bins) ^a	Hourly (120 × 1 Hz ensemble)
150 kHz ADCP ^b	35–150 m (8 m bins)	Hourly (45 × 0.0125 Hz ensemble)

^aPartial data availability (see section 2.2).

^bEnhanced monitoring period.

(dSSTa), ω the diurnal frequency, $\Phi(t)$ the phase, and $Z(t)$ variability at other frequencies. The peak-to-peak diurnal SST range will thus be, $2 \times \text{dSSTa}$. Diurnal SST maxima occur near 1400 Local Time (LT) throughout the record, so we do not discuss the phase information, $\Phi(t)$, further. An alternate estimate of dSSTa was formed by directly differencing daily maxima and minima after removing low-frequency trends (following Cronin and McPhaden [1999]). Estimates of monthly averaged dSSTa from the two methods are highly correlated ($r = 0.99$), with regression analysis indicating a slight bias (17%) toward higher values of dSSTa using the differencing method. We thus proceed with complex demodulation as providing a conservative estimate of diurnal SST variability (uncertainty estimates for dSSTa are discussed in Appendix A).

Figure 2a shows the clear seasonal cycle in monthly averaged dSSTa. Maximum values are found in boreal winter and spring, with typical diurnal SST ranges of 0.5–0.6°C (dSSTa of 0.25–0.3°C), consistent with estimates for this location derived from modeling and remote sensing studies [Stuart-Menteth et al., 2003; Bernie et al., 2007; Clayson and Weitlich, 2007]. In boreal summer and fall, the diurnal SST range is reduced to 0.2–0.3°C (dSSTa of 0.1–0.15°C). The seasonal cycle of dSSTa covaries inversely with the seasonal cycle of wind stress (Figures 2b and 3), reflecting the mixing of surface heat fluxes through deeper diurnal mixed layers during periods of enhanced wind stress, as discussed in section 4 [Price et al., 1986; Brainerd and Gregg, 1993; Cronin and Kessler, 2002].

PIRATA temperature measurements have finer vertical resolution, and fewer data gaps, than salinity measurements, so for the full time series we define an isothermal mixed layer depth (MLD_T) as the depth at which temperature is 0.4°C less than the 1 m temperature, which is approximately equivalent to a density change of 0.125 kg m^{-3} (Figure 2d). Alternate definitions of MLD_T were tested with similar results. The calculation of MLD_T is not linear with respect to temporal averaging, so we calculate MLD_T first using daily temperature values linearly interpolated to a 1 m grid, and subsequently take the monthly average. Additional measures of near-surface stratification are the depth of the 20°C isotherm, a proxy for the thermocline depth (Figure 2d), and the near-surface thermal stratification (ΔT), which we define as the difference between temperature observations at 1 and 5 m (Figure 2c).

Consistent with the seasonal cycle in dSSTa, these measures of near-surface stratification all exhibit a seasonal cycle driven by seasonal changes in wind stress. Wind speeds are at their maximum in boreal summer and fall, and the near-surface layer is well mixed with deep MLD_T and thermocline, and low ΔT . As the wind speed begins to drop in boreal winter, the mixed layer shoals rapidly, and near-surface stratification and dSSTa increase. The thermocline also begins to shoal in boreal winter; however, its response is often slower than MLD_T , with minimum thermocline depths occurring later in the seasonal cycle. This time lag reflects the basin-scale dynamics involved in setting the depth of the equatorial thermocline, which linear theory predicts will respond to the zonally integrated wind stress [McPhaden, 1993], whereas MLD_T responds rapidly to local forcing.

alternate approaches for filling missing salinity observations, as well as density calculations based solely on temperature, were tested.

3. Seasonal Cycle

SST variance at the diurnal frequency is isolated using complex demodulation. This technique expresses a signal as a linear combination of a component oscillating at the frequency of interest, with slowly varying amplitude and phase, and additional variability at other frequencies which is removed by filtering [Bloomfield, 1976]. Complex demodulation is applied to the 1 m temperature observations, T_{1m} , giving,

$$T_{1m}(t) = A(t)\cos(\omega t - \Phi(t)) + Z(t)$$

where $A(t)$ is the diurnal SST amplitude

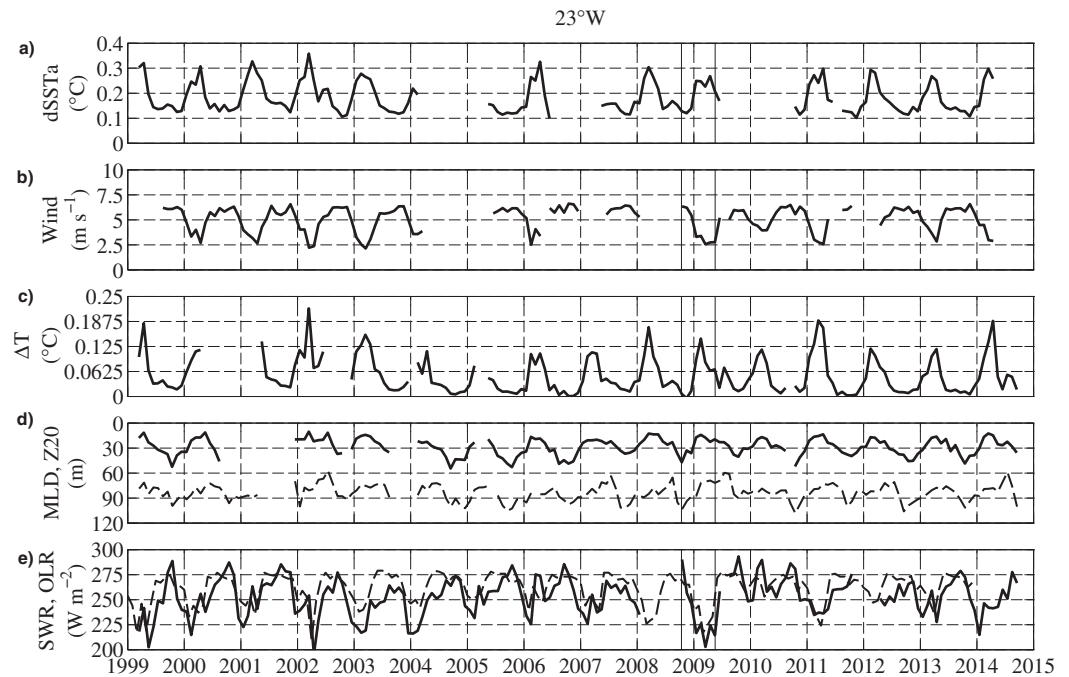


Figure 2. Overview of the full monthly averaged time series. (a) Diurnal SST amplitude (dSSTa), (b) wind speed, (c) thermal stratification ($\Delta T = T_{1m} - T_{5m}$), (d) isothermal mixed layer depth (solid line, $\Delta T = 0.4^\circ\text{C}$) and depth of the 20°C isotherm (dashed line), (e) downwelling shortwave radiation (solid line) and top of atmosphere outgoing longwave radiation (dashed line) [Liebmann and Smith, 1996]. Solid vertical lines denote the enhanced monitoring period (section 4).

A monthly climatology, formed from all available data, is shown in Figure 3. The annual pattern of monthly averaged wind stress and SWR reflects the seasonal meridional migration of the ITCZ in the Atlantic (Figure 1) [Waliser and Gautier, 1993]. As the ITCZ shifts south during late boreal fall and winter, SWR and wind speed both decrease. dSSTa reaches an annual monthly averaged maximum of 0.28°C in March, despite shortwave radiation (SWR) being 31 W m^{-2} below its October maximum. Later in the year, the ITCZ shifts further north of the equator, leading to clear skies and steady trade wind conditions, associated with low dSSTa. This climatology suggests available surface heat flux is secondary to near-surface mixing in setting the diurnal SST amplitude, with reduced wind stress, shallow mixed layers, and increased stratification during boreal winter linked to larger near-surface diurnal SST signals. The precise mechanisms responsible for variations in dSSTa will be discussed further using data from the EMP in section 4.

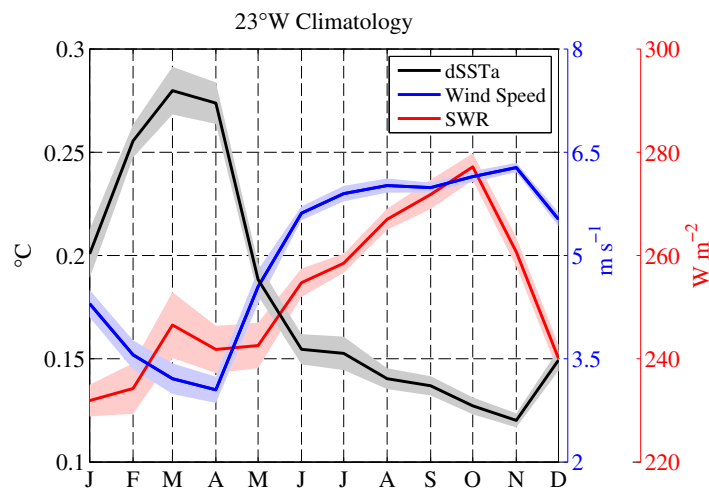


Figure 3. Monthly averaged climatology for diurnal SST amplitude (black line), wind speed (blue line), and shortwave radiation (red line). Shading denotes \pm one standard error of the monthly mean.

Interannual variability in the Atlantic is weak compared to the seasonal cycle [Xie and Carton, 2004], and interannual anomalies of dSSTa at 0° , 23°W are of smaller amplitude than those in the Pacific [Clayson and Weitlich, 2007]. Using similar moored data at 0° , 110°W , Cronin and Kessler [2002] observed interannual variability of the diurnal SST amplitude on the order of $\pm 0.1^\circ\text{C}$

associated with the El-Niño Southern Oscillation. The primary modes of interannual variability in the tropical Atlantic are the Atlantic meridional mode and the zonal Atlantic Niño mode [Servain, 1991; Zebiak, 1993]. Although the time range of observations covers both positive and negative Atlantic meridional mode and Atlantic Niño events, we do not observe monthly average dSSTa values exceeding $\pm 0.05^\circ\text{C}$ from the climatological values.

4. Enhanced Monitoring Period

Atmosphere and ocean conditions during the 8 month EMP are summarized in Figure 4. The EMP began in October 2008, during a regime characterized by steady southeast trade winds, limited precipitation, and average dSSTa of 0.13°C . In early January, winds became lighter and more variable in direction, and there was more frequent rain and cloudiness (Figures 4b and 4c), with significant variance of dSSTa on sub-monthly time scales. This basic seasonality is consistent with the climatology (Figure 3), although in boreal spring 2009 the ITCZ shifted anomalously far south due to a strong negative AMM event, leading to negative anomalies in wind speed magnitude (-1 m s^{-1}) and SWR (-30 W m^{-2}) at $0^\circ, 23^\circ\text{W}$, as well as anomalously high sea surface height and SST across the equatorial basin [Foltz and McPhaden, 2010; Foltz et al., 2012]. After the period of variable winds, steady trade winds were reestablished, followed by a dramatic 5°C cooling of the cold tongue region between June and August attributed to upwelling dynamics [Foltz and McPhaden, 2010]. Conditions during boreal spring 2009 are thus not entirely representative of a typical year, although the limited dSSTa anomalies during this period (Figure 2) suggest that diurnal variability may not have been as strongly atypical.

Zonal velocity is dominated by the strong eastward-flowing undercurrent in the thermocline exceeding 1 m s^{-1} , with the westward South Equatorial Current above it in the surface layer. This results in a high shear region on the upper flank of the undercurrent core below the mixed layer (MLD), which is defined during the EMP as the depth at which density first exceeds the 1 m value by 0.01 kg m^{-3} . The limited vertical resolution of the PIRATA mooring adds uncertainty to the calculation of MLD; however, this criteria was found to best identify the diurnal mixed layer based on visual inspection of density profiles, was highly correlated with other more generous definitions of MLD, and provides consistency with prior work [Brainerd and Gregg, 1995]. Meridional velocity is generally small, except during the passage of several tropical instability waves (TIWs) in the early part of the record, evident in the alternating north-south flow with period of approximately 30 days [Legeckis, 1977; Grodsky et al., 2005]. Below the mixed layer, buoyancy frequency squared ($N^2 = -\rho^{-1}g\rho_z$) increases downward toward the thermocline, with near-surface enhancement during the southward phase of a TIW in November 2008.

To quantify the likelihood of shear-driven mixing, we use reduced shear squared, defined as,

$$S_{red}^2 = u_z^2 - 4N^2$$

where u_z is the vertical shear of horizontal currents. To account for uneven spacing of temperature, salinity, and velocity observations, S_{red}^2 is calculated using first differences with a vertical separation of 5.25 m between 3.75 and 30 m , and 10 m separation below 30 m . Errors in the calculated values of S_{red}^2 can arise from a variety of sources, including instrument noise, horizontal separation between the deep ADCP and temperature and salinity measurements, and the coarse vertical resolution. These sources of error are addressed in Appendix B, and while they introduce significant uncertainty into the hourly estimates of S_{red}^2 , they do not alter the basic interpretation of the statistics used in this analysis.

S_{red}^2 is simply a rearrangement of the Richardson number ($Ri = N^2 u_z^{-2}$), such that when $S_{red}^2 > 0$, $Ri < 0.25$. Thus, when S_{red}^2 is positive it implies flow regimes that are unstable to shear instabilities, whereas negative values imply stability. For our purposes, characterizing the flow as stable or unstable, S_{red}^2 is preferable to Richardson number as it linearizes the effect of observational errors in velocity shear, its distribution is less skewed than the Richardson number, and it retains additional information about the kinetic energy of the flow [Hazel, 1972; Kunze et al., 1990; Sun et al., 1998]. It is worth noting that the true stability boundary for stratified shear flows is not solely a function of the Richardson number, and may depend on the turbulent Reynolds number, as well as preexisting turbulence in the flow [Smyth et al., 2013]. However, defining a critical value of $Ri = 0.25$ ($S_{red}^2 = 0$) is a common and useful first approximation.

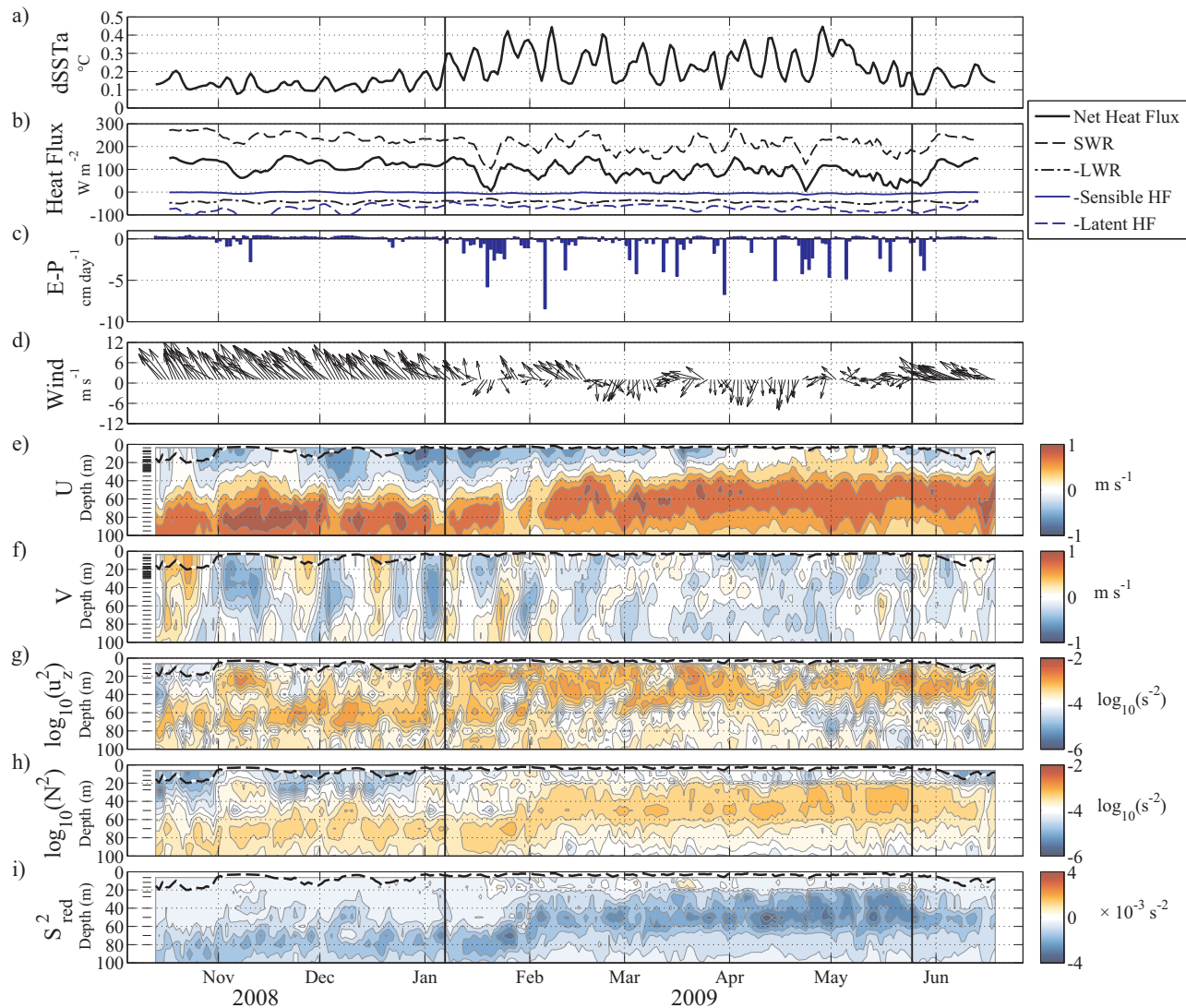


Figure 4. Overview of atmosphere and ocean conditions during the EMP using daily averaged data. (a) Diurnal SST amplitude ($dSSTa$) smoothed with a 5 day moving average, (b) smoothed net surface heat flux (solid black line) defined positive into the mixed layer with components as indicated in the legend, (c) evaporation minus precipitation, (d) wind vectors (magnitude indicated by vector length with scale on the ordinate, direction indicated by vector orientation with north up), (e) zonal velocity, (f) meridional velocity, (g) $\log_{10}(u_z^2)$, (h) $\log_{10}(N^2)$, and (i) median daily S_{red}^2 . For Figures 4e–4i, dashed black line shows MLD, and measurement depths are indicated by tick marks inside the left axis. Vertical black lines indicate the two compositing regimes discussed in section 4.

Throughout the EMP, S_{red}^2 is elevated between the surface and the thermocline, due to high near-surface shear and low near-surface stratification. During steady trade wind conditions, there is an approximately 40 m thick layer below the mixed layer where $S_{red}^2 \approx 0$, indicating marginal instability and potentially active deep-cycle turbulence [Smyth and Moum, 2013], which is discussed further in section 5. A thinner marginally stable layer, approximately 15 m thick, persists throughout the variable wind conditions, following the shoaling of the equatorial undercurrent and thermocline (Figure 4i).

A sample 7 day period of hourly data, taken when the trades were relatively steady during the cold phase of a TIW, clearly demonstrates the diurnal cycle of near-surface shear and stratification (Figure 5). The daily cycle of solar insolation leads to rapid morning shoaling of the mixed layer, and increasing thermal stratification that begins at the surface, and penetrates deeper into the water column as the day progresses. This thermal stratification inhibits the vertical transfer of momentum from the wind, leading to intensified near-surface shear [Price et al., 1986; Bond and McPhaden, 1995]. Beginning between 1200 and 1400 LT, the mixed layer begins to deepen. This occurs before the surface heat flux has changed sign, and is associated with positive values of S_{red}^2 , suggesting shear instability as a mechanism for this deepening. While there is

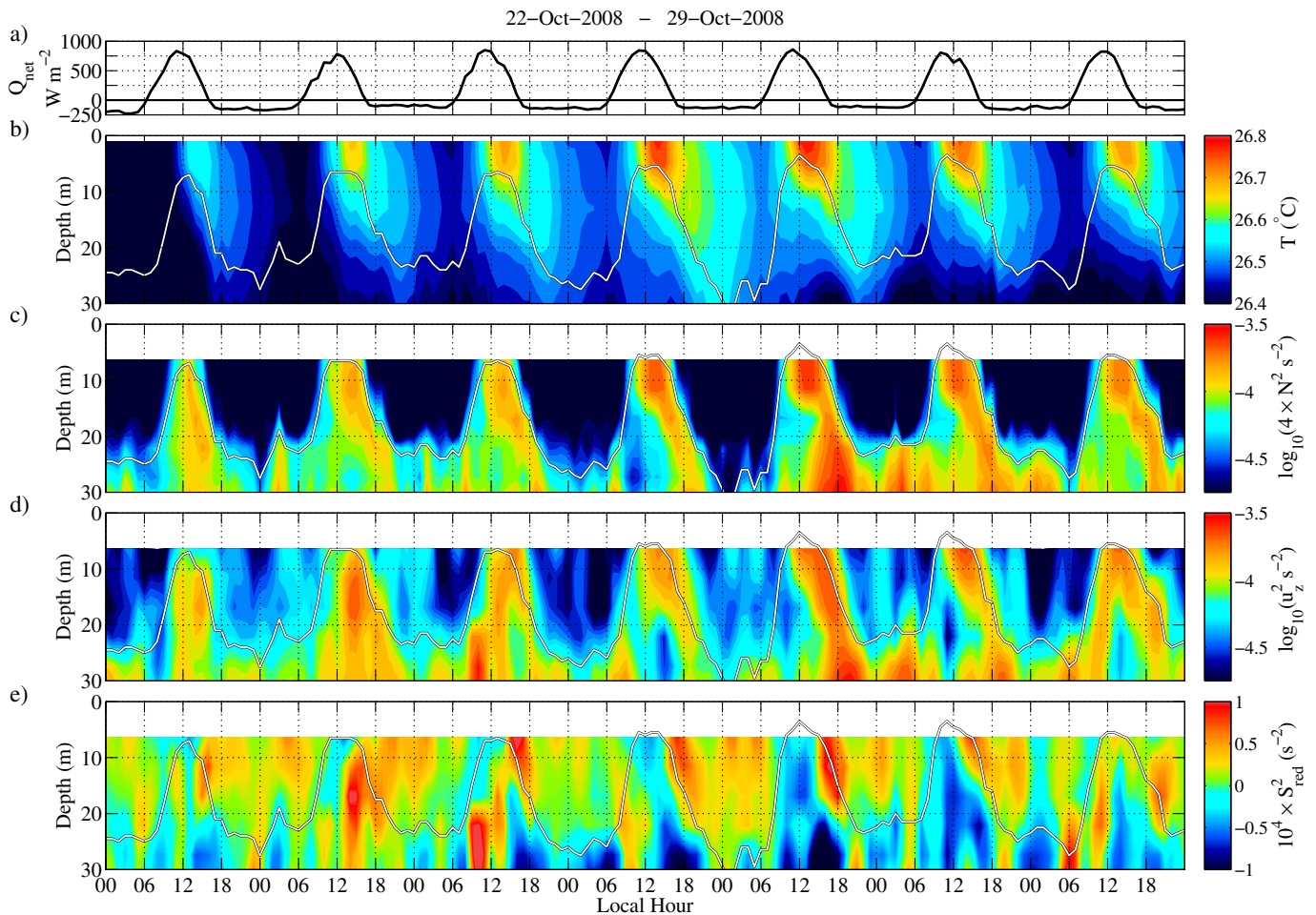


Figure 5. Sample hourly time series of the diurnal shear layer. (a) Net surface heat flux, (b) subsurface temperature, (c) $\log_{10}(4 \times N^2)$ multiplied to facilitate comparison with shear, (d) $\log_{10}(u_z^2)$, and (e) S_{red}^2 . Figures 5d and 5e are smoothed with a 1–2–1 filter in time and depth to improve presentation clarity; solid line in Figures 5b–5e denotes the MLD.

significant temporal and spatial variability, as well as uncertainty, in our hourly estimates of S_{red}^2 , this picture is qualitatively similar to recent observations from the Pacific, where descending diurnal shear layers associated with subcritical Richardson numbers were shown to provide an initiation mechanism for deep-cycle turbulence [Smyth *et al.*, 2013].

In order to further examine the dynamics of the diurnal mixed layer, we divide the EMP into two regimes. The early part of the record is characterized by relatively steady trade winds, clear skies, deep mixed layers and thermocline, and marginal instability of the upper equatorial undercurrent. In contrast, the latter part of the record exhibits weaker and more variable winds, frequent cloudiness and precipitation, shallow mixed layers, and a shoaling of the undercurrent and thermocline. Diurnal composites for these two regimes are described in the following two sections.

4.1. Steady Trade Wind Conditions

A composite diurnal cycle over the upper 30 m is formed by phase averaging hourly observations from 13 October 2008 to 6 January 2009. Wind stress and horizontal currents are vector averaged, and horizontal currents referenced to the 20 m values, giving the sheared component of the flow. Temperature observations are phase averaged, and the time–depth mean removed to give the diurnal anomaly. We define an eddy viscosity, A_v , using the shear-stress surface boundary condition, $\rho A_v u_z = \tau$, where ρ is the density of seawater, u_z is the vertical shear magnitude, and τ is the surface wind stress magnitude. This can be rearranged to give an equation for A_v [Santiago-Mandujano and Firing, 1990; Wenegrat *et al.*, 2014],

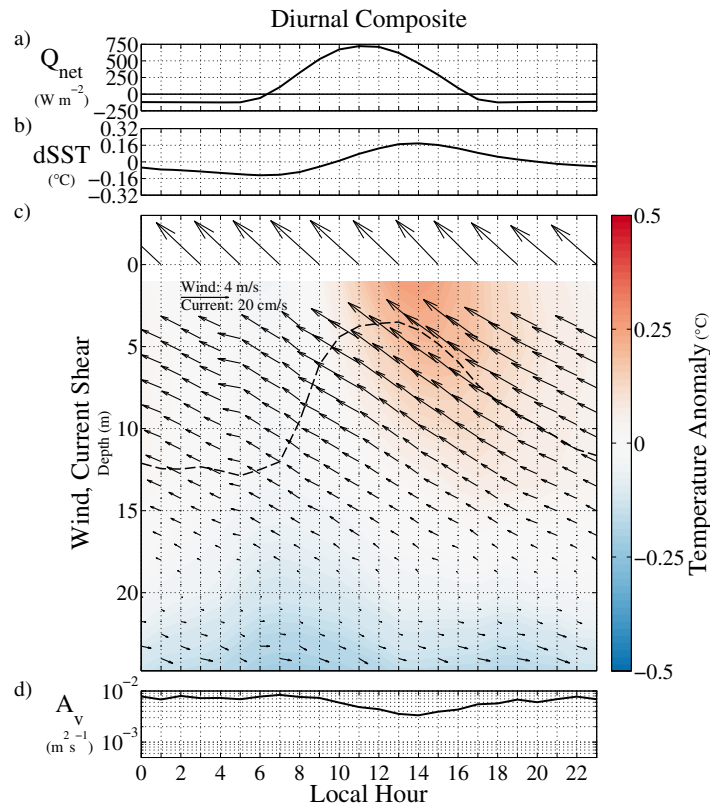


Figure 6. Composite diurnal cycle during steady trade wind conditions (section 4.1). (a) Net surface heat flux, (b) SST anomaly, (c) wind vectors plotted along the $z = 0$ line, current vectors (relative to the 20 m currents) plotted at their observation depths (vectors are oriented with north up, and magnitude scale is shown in upper left), also plotted are the temperature anomaly (relative to the time-depth average, color scale), and MLD (dashed line), (d) eddy viscosity, calculated as discussed in section 4.1.

Figure 6 shows the diurnal composite for the steady trade wind period. Surface heat flux becomes positive into the mixed layer shortly after 0600 LT, leading to a rapid shoaling of the mixed layer from 13 to 3.5 m. Near-surface temperature begins to rise, and a diurnal jet develops in the downwind direction. At 1400 LT, SST reaches its maximum diurnal amplitude of $0.18^{\circ}C$ and shortly after, at 1500 LT, surface shears reach 20 cm s^{-1} relative to the 20 m currents. As there is limited diurnal variance in the wind, the afternoon maximum of near-surface shear is associated with a daily minimum of $A_v = 3.3 \times 10^{-3} \text{ m}^2 \text{ s}^{-1}$, reduced more than a factor of 2 from nighttime values [Wenegrat et al., 2014]. In the late afternoon, the mixed layer begins to deepen, A_v increases, and diurnal temperature anomalies are spread over an increasingly deep mixed layer, limiting the magnitude of the dSSTa, as noted in section 3 [Price et al., 1986; Bond and McPhaden, 1995].

Composites of S_{red}^2 are presented in terms of the fraction of hourly observations in each time-depth bin that are unstable to shear instability ($S_{red}^2 > 0$; Figure 7), which we denote as $\mathcal{F}(S_{red}^2)$. During steady trade wind conditions, there is a clear diurnal cycle of S_{red}^2 , with an increasingly stable near-surface layer formed at the surface and penetrating deeper into the layer as the day progresses. Minimum daily values of $\mathcal{F}(S_{red}^2)$ are found at 1000 LT at 6.37 m depth, and at 1900 LT at 22.12 m depth. $\mathcal{F}(S_{red}^2)$ increases throughout the afternoon, and by 1600 LT, shortly before the surface heat flux changes sign, approximately 40% of observations in the upper 20 m have unstable values of S_{red}^2 . The deepening of the mixed layer, which begins midday, along with increased $\mathcal{F}(S_{red}^2)$, suggest that shear instabilities may be forming in the diurnal shear layer. After the surface heat flux changes sign the mixed layer continues to deepen, and $\mathcal{F}(S_{red}^2)$ increases as a result of convective mixing.

4.2. Variable Wind Conditions

The diurnal composite formed during the period of variable wind forcing, 7 January 2009 to 24 May 2009 exhibits a very different evolution (Figure 8). Consistent with the climatological pattern (Figure 3) maximum

$$A_v = \frac{\tau}{\rho u_z}, \quad z=0$$

We evaluate this using the uppermost valid velocity observations, giving a nominal shear depth of 5.64 m. This approach can be treated as an assumption of uniform stress between the surface and 5.64 m, and thus the value of A_v we infer will be approximate. It can be considered analogously to the mixing length scaling of Prandtl, which defines a mixing length, l , based on dimensional considerations as the ratio between friction velocity, $u_* = (\tau \rho^{-1})^{1/2}$, and shear, $l = u_* u_z^{-1}$ [Stull, 1950]. Thus, $A_v = l^2 u_z$. The distribution of A_v is highly skewed, with a small number of very large values occurring as $u_z \rightarrow 0$, and hence values which exceed the 99th percentile ($A_v \geq 0.045 \text{ m}^2 \text{ s}^{-1}$), estimated using the bootstrap method [Efron and Tibshirani, 1993], are excluded prior to compositing using the geometric mean.

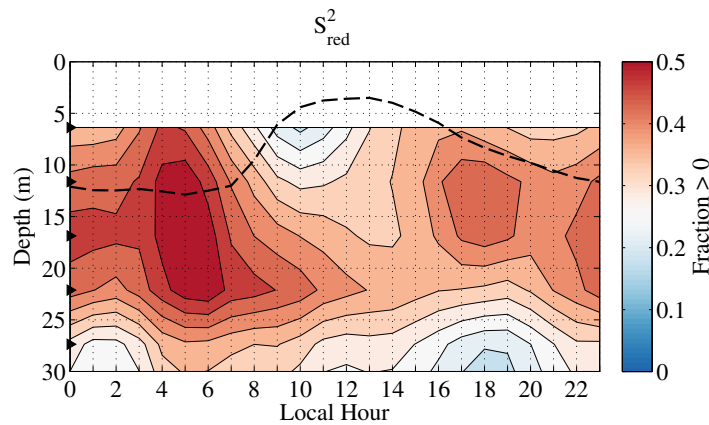


Figure 7. Fraction of diurnal composite observations during the steady trade wind conditions (section 4.1) for which $S_{red}^2 > 0$, indicating flow unstable to shear instabilities. S_{red}^2 bin center points are indicated with black triangles on the ordinate, and average MLD is plotted with the dashed line. Bins are smoothed with a 1-2-1 filter in time and depth to improve presentation clarity.

cycle, indicating less near-surface mixing than during steady wind conditions. Despite the absence of strong wind forcing, the near-surface layer remains highly sheared below the mixed layer, resulting from the shallow equatorial undercurrent.

Above 20 m, S_{red}^2 undergoes a diurnal cycle (Figure 9) controlled by changes in stratification (Figure 8). During daytime hours, the near-surface layer becomes increasingly stable, with the daily minimum $\mathcal{F}(S_{red}^2)$ persisting until 1400 LT, much later than during the steady wind conditions. A predawn enhancement of $\mathcal{F}(S_{red}^2)$, similar to that observed during the steady trade wind conditions, can be attributed to nighttime

net heat flux is reduced by 128 W m^{-2} , and wind speed by 2.7 m s^{-1} , compared to the steady trade wind conditions. Diurnal temperature variations are strongly surface trapped, with peak diurnal SST amplitude reaching 0.3°C at 1400 LT and persisting later in the day than during steady wind conditions. Corresponding to this, the mixed layer remains shallow throughout both day and night and does not display the rapid afternoon deepening seen in the stronger wind conditions. A_v is reduced to approximately $10^{-3} \text{ m}^2 \text{ s}^{-1}$ and lacks a significant diurnal

convective mixing that decreases near-surface stratification. Below 20 m, isopleths of $\mathcal{F}(S_{red}^2)$ show only a slight diurnal cycle, suggesting limited vertical penetration of surface-forced diurnal anomalies.

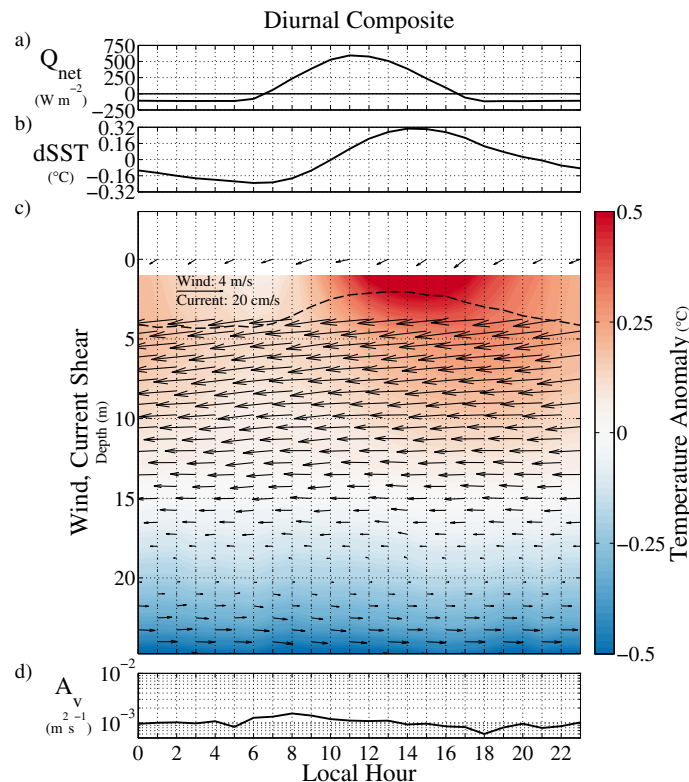


Figure 8. As in Figure 6, for the variable wind period (section 4.2).

4.3. Tropical Instability Waves

After the seasonal cycle, the most prominent timescale of variability during the EMP is that associated with the passage of several TIWs from October through January (Figure 4f). During TIWs, alternating north-south meridional flow with period of approximately 30 days advects the background SST gradient (Figure 1) and modifies near-surface S_{red}^2 through changes in both u_z and N^2 [Weisberg and Weingartner, 1988; Jochum et al., 2004; Grodsky et al., 2005; Moum et al., 2009]. TIWs

are also known to modulate equatorial turbulence [Lien *et al.*, 2008; Moum *et al.*, 2009], with enhanced mixing during the transition from north (cold SST) to south (warm SST) phases [Lien *et al.*, 2008; Inoue *et al.*, 2012]. In our data, winds remain relatively steady across TIW phases (see Chelton and Xie [2010] for a discussion of TIW-atmosphere coupling), and while TIWs change the local SST, there is only limited TIW modulation of dSSTa (Figure 4a) [Cronin and Kessler, 2002]. However, subsurface conditions differ dramatically by TIW phase, as is evident in Figure 10, which shows the passage of a TIW, beginning in the cold (north) phase, progressing into the warm (south) phase around 31 October, and then returning to a cold phase around 16 November.

During the cold phases, diurnal cycling of the MLD is pronounced, with nighttime mixed layers reaching 20–40 m and daytime mixed layers shoaling to less than 5 m. Stratification and shear are enhanced along the base of the mixed layer, and a layer of elevated S_{red}^2 extends from the mixed layer toward the core of the undercurrent in the thermocline. In the warm phase of the TIW, SST warms by approximately 1.5°C (Figure 10b), and there is a reduction in net surface heat flux (Figure 10a). During this phase of the TIW, the diurnal SST anomaly does not change appreciably from the cold phase. However, a subsurface diurnal cycle is less evident, with a consistently shallow mixed layer and a less clearly defined diurnal cycle of S^2 , potentially due to our inability to resolve velocity above 3.75 m.

Additionally, during the warm phase, the layer of enhanced S_{red}^2 below the mixed layer bifurcates into two distinct layers, separated by a thin region of stable S_{red}^2 centered at approximately 40 m depth. Moum *et al.* [2009] first noted this feature in the tropical Pacific, and termed the lower of these layers the upper core layer. They found the upper core layer continued to show enhanced turbulent dissipation, but appeared to be dynamically isolated from the surface-forced diurnal cycle. While qualitatively similar to the upper core layer observed in the Pacific, the layer observed here is thinner, and does not appear as distinctly isolated from the near-surface layer of elevated shear, potentially due to the shallower thermocline at this location or our lower resolution observations [Inoue *et al.*, 2012]. We also observe an enhancement of S_{red}^2 at the base of the deep-cycle layer during the cold phase, due in part to enhanced meridional shear.

The composite diurnal cycle of section 4.1 will average across TIWs, so here we segment by TIW phase. The 0°, 23°W mooring does not evenly sample all TIW phases, being offset to the south from the center of the TIW wave midline, as determined from satellite SST imagery. Hence, we divide the observations into only two phases, a cold phase on 15 October to 30 October, and a warm phase from 31 October to 15 November.

In the cold phase of the wave, S_{red}^2 undergoes a very clearly defined diurnal cycle (Figure 11a). The nighttime near-surface layer has low stratification, and 86% of observations at 5.26 m have $S_{red}^2 > 0$ at 0300 LT. Following dawn, the upper water column rapidly stabilizes due to thermal stratification. The afternoon increase of shear, leading to increased $\mathcal{F}(S_{red}^2)$, that was discussed in section 4.1 is even more clearly defined during the TIW cold phase. At 1300 LT, the mixed layer begins to deepen, along with rapidly increasing $\mathcal{F}(S_{red}^2)$, suggesting that shear instabilities are eroding the diurnal thermal stratification.

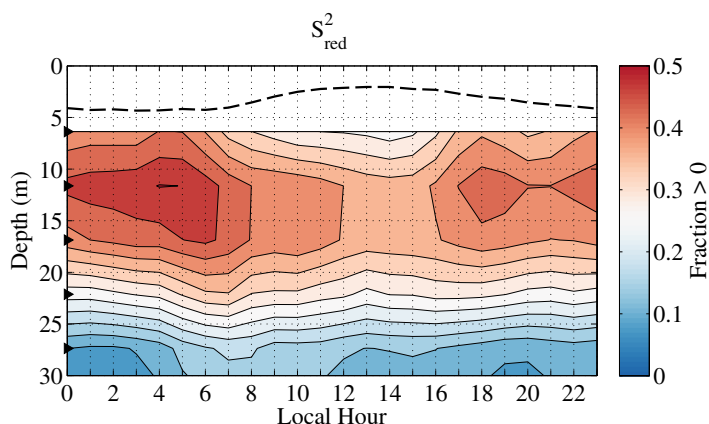


Figure 9. As in Figure 7, for the variable wind period (section 4.2).

The composite diurnal cycle is very different during the warm phase of the TIW, where the warmer, more strongly stratified, near-surface layer is more stable throughout the diurnal cycle (Figure 11b). $\mathcal{F}(S_{red}^2)$ is reduced at all hours, and only a weak diurnal cycle of S_{red}^2 is apparent above 15 m depth. However, the low dSSTa during this phase of the TIW suggests that a similar wind-driven mixing is continuing to occur in the shallow mixed layer above our observation depths, with

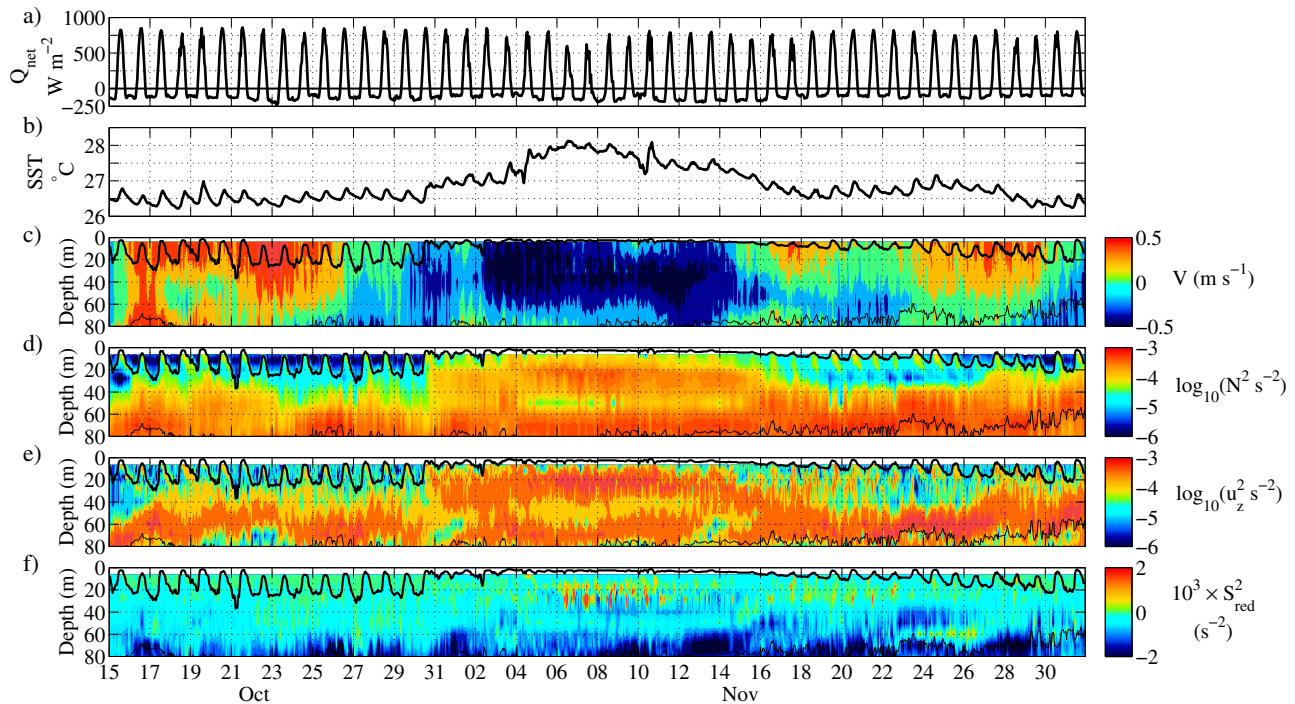


Figure 10. Overview of hourly observations during the passage of a TIW. (a) Net surface heat flux, (b) SST, (c) meridional velocity, (d) $\log_{10}(N^2)$, (e) $\log_{10}(u_z^2)$, and (f) S_{red}^2 . For Figures 10c–10f, the MLD is shown in heavy black line, and the depth of the 1025 kg m^{-3} isopycnal is shown in light black line.

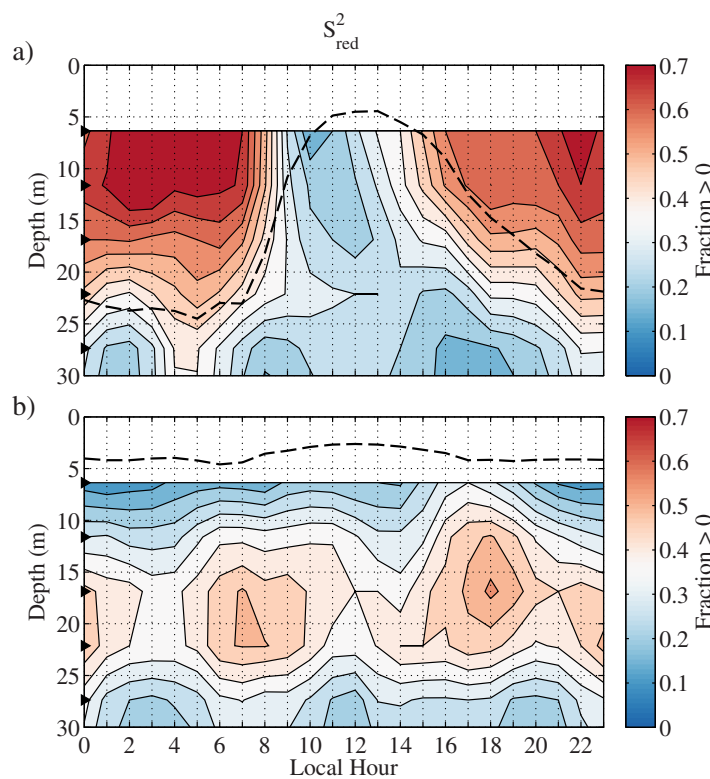


Figure 11. As in Figure 7, for (a) TIW cold phase from 15 October to 30 October, (b) TIW warm phase from 31 October to 15 November. Note modified color scale relative to Figure 7.

limited vertical penetration of the diurnal shear layers.

5. Marginal Instability

Recent work using long moored measurements of dissipation at $0^\circ, 140^\circ\text{W}$ suggests that flows with Richardson numbers distributed around the critical value of 0.25, a form of statistical equilibrium termed marginal instability, may indicate regimes where deep-cycle turbulence is active [Thorpe and Liu, 2009; Smyth and Moum, 2013]. While the existence of marginal instability does not quantify the strength of turbulence, it is particularly well suited to evaluation from moored records. Smyth and Moum [2013] demonstrate that increasing the vertical separation over which Richardson number is calculated alters the skewness of

the resulting distribution, but does not eliminate the distribution’s peak near the critical value. Consequently, marginal instability continues to be clearly identifiable regardless of vertical scale. Deep-cycle turbulence is one of the defining features of the diurnal cycle on the equator and, as we lack direct measurements of dissipation, we can use measures of marginal instability as a proxy for the existence of active deep-cycle turbulence.

Figure 12 shows median profiles of S_{red}^2 for the two wind forcing regimes, as well as the distribution of observations in the 22–50 m depth range. During steady trade wind conditions, there is a 40 m thick layer below the mixed layer where $S_{red}^2 \approx 0$, while during variable wind conditions this same layer becomes increasingly stable with depth. This is further illustrated in Figure 12b, where the distribution of S_{red}^2 is sharply peaked around 0 for the steady trade wind conditions, while it is skewed toward more negative (stable) values when the winds are light and variable. Figure 12c shows this same shift in distribution in terms of Richardson number. This shift in the stability of the equatorial undercurrent layer below the mixed layer suggests a seasonal cycle in deep-cycle turbulence, which is discussed further below.

Additional shorter time scale variability in the stability of the near-surface layer is also distinguishable in Figure 4i. Notably, the thick layer of $S_{red}^2 \approx 0$ below the mixed layer during steady wind conditions persists into late January, well after the change in local wind stress, and cessation of the strong diurnal cycle of shear flow. This occurs coincident with the south phase of a TIW (Figure 4f), with a large component of the total shear coming from shear in the 20–40 day period band, including significant contributions from the meridional component. This enhanced shear, along with a deep thermocline, contributes to the persistence of marginal instability above 50 m, despite the absence of strong local surface forcing and diurnal shear layers.

Estimates of the turbulent dissipation rate, ϵ , below the mixed layer can be formed using parameterizations based on S_{red}^2 or Richardson number. While a comparison of dissipation parameterizations is beyond the

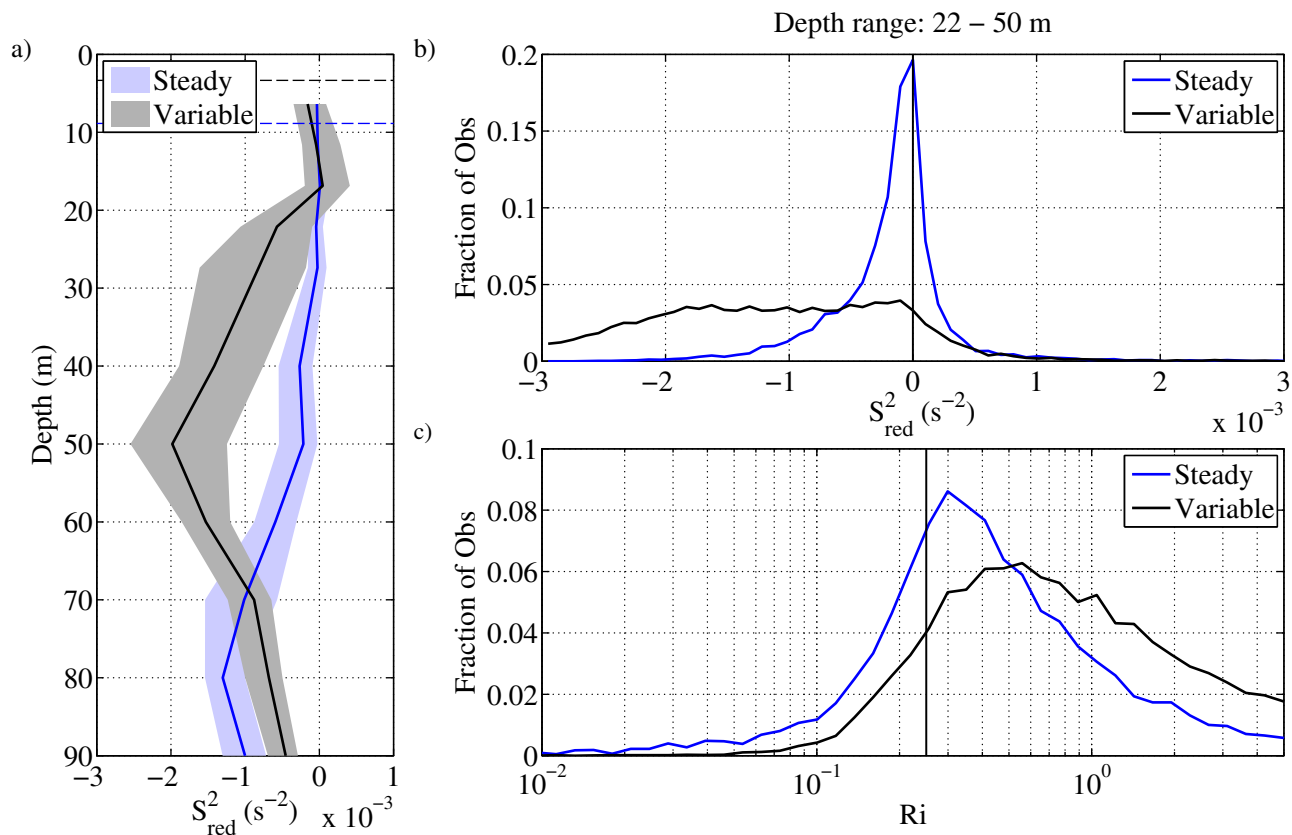


Figure 12. Marginal instability (MI) by time period. (a) Median S_{red}^2 (solid line) with interquartile range (shaded), (b) distribution of S_{red}^2 for observations between 22 and 50 m depth, (c) as in Figure 12b, but for Richardson number ($Ri = N^2 u_z^{-2}$). Dashed horizontal lines in Figure 12a indicate the mean MLD; solid vertical lines in Figures 12b and 12c indicate the critical value for stability.

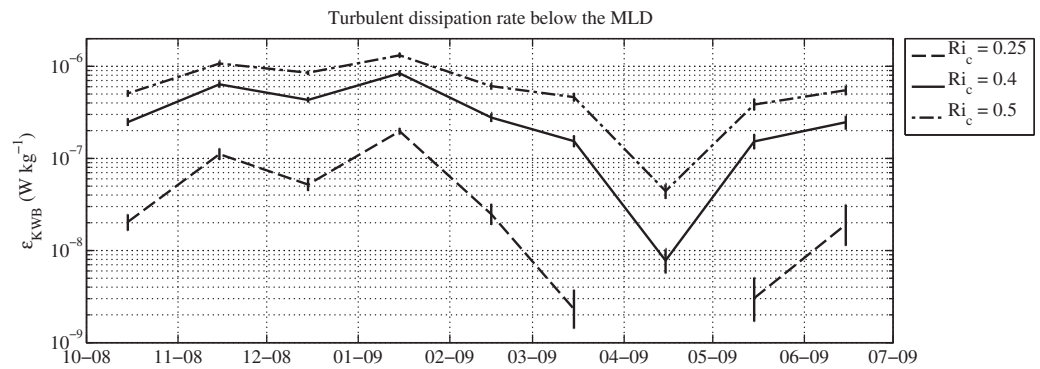


Figure 13. Monthly averaged (5% trimmed) turbulent dissipation rates, ϵ_{KWB} (W kg^{-1}), over the layer 20–50 m below the hourly MLD. Estimates are calculated for three different values of Ri_c as indicated in the legend. The trimmed mean for April ($Ri_c=0.25$) equals 0 and is not plotted. These results from the definition of the *Kunze et al.* [1990] parameterization, which equals zero whenever the instability criteria are not met (section 5). Vertical error bars indicate 95% confidence intervals on the trimmed mean, estimated using the bootstrap method.

scope of the present work, for completeness we apply the turbulence parameterization of *Kunze et al.* [1990] to provide a quantitative estimate of the turbulent mixing implied by the marginal instability noted above. This parameterization is based on the energetics of Kelvin-Helmholtz instabilities, and gives

$$\epsilon_{KWB} = \frac{\Delta z^2}{96} \left\langle u_z^2 - \frac{N^2}{Ri_c} \right\rangle \left\langle u_z - \frac{N}{\sqrt{Ri_c}} \right\rangle$$

where $\langle x \rangle = 0$ if $x \leq 0$ and $\langle x \rangle = x$ for $x > 0$, and Δz is the vertical separation over which u_z and N are calculated [*Kunze et al.*, 1990; *Peters et al.*, 1995; *Polzin*, 1996]. The critical Richardson number, Ri_c , was assumed in *Kunze et al.* [1990] to be 0.25; however, it may also be treated as a free parameter to account for observational constraints such as vertical resolution [*Polzin*, 1996]. We present results for several possible choices of Ri_c (Figure 13), with $Ri_c=0.4$ suggested based on the vertical scale of our observations [*Polzin*, 1996]. Ocean turbulence statistics are highly skewed [*Peters and Gregg*, 1988]; hence, estimates of average ϵ_{KWB} are formed using the trimmed mean, excluding the highest and lowest 5% of hourly observations before averaging, which provides a robust estimator of central tendency for heavy-tailed distributions [*Wilcox*, 2010].

Calculated values of ϵ_{KWB} demonstrate a seasonal cycle of turbulence, regardless of choice of Ri_c , with elevated ϵ_{KWB} during the steady trade wind conditions, and values decreasing by 1–2 orders of magnitude during the variable wind regime in boreal spring (Figure 13). We note that ϵ_{KWB} is enhanced at high S_{red}^2 and thus also follows a diurnal cycle similar to that discussed in section 4. The seasonal modulation of turbulent dissipation, and marginal instability, below the mixed layer indicates a seasonal cycle of deep-cycle turbulence in the central Atlantic broadly consistent with estimates derived from heat budgets at this location [*Foltz et al.*, 2003; *Hummels et al.*, 2014], and similar to the seasonal cycle of dissipation observed at 0° , 10°W in the eastern Atlantic [*Hummels et al.*, 2013], and at 0° , 140°W in the Pacific [*Moum et al.*, 2013; *Smyth and Moum*, 2013]. Further, these finding suggests in-phase seasonal variability of the marginally unstable layer and the prominence of diurnal shear layers.

6. Summary

We have provided an assessment of diurnal SST, near-surface shear, and stratification at 0° , 23°W in the central equatorial Atlantic using a 15 year time series in conjunction with an 8 month enhanced monitoring period of high-vertical resolution velocity observations. Major results can be summarized as follows:

1. The diurnal cycle of SST in the central equatorial Atlantic is strongly modulated by wind stress, with climatological monthly mean diurnal SST amplitude reaching 0.28°C during the light and variable wind conditions prevalent in boreal winter and spring. Climatologically, the highest diurnal range in SST occurs during periods of reduced SWR, suggesting that wind-driven mixing determines the seasonal modulation of diurnal SST amplitude. Interannual variability of diurnal SST amplitude at this location is small compared to the seasonal cycle.

2. During relatively steady trade wind conditions, we regularly observe descending diurnal shear layers, corresponding to an increased frequency of $S_{red}^2 > 0$ ($Ri < 0.25$). The mixed layer frequently begins to deepen while the surface heat flux is still into the ocean, suggesting that instabilities of the sheared diurnal jets are mixing the near-surface layer. This mixing reduces the maximum achievable diurnal SST amplitude by spreading heat over deeper layers. During light and variable wind conditions, we see a near-surface diurnal cycle of S_{red}^2 , resulting primarily from diurnal variability of N^2 . Mixed layers are shallow and diurnal temperature anomalies are strongly surface trapped, resulting in larger diurnal SST signals.
3. TIWs modulate the diurnal cycle in the mixed layer of the tropical Atlantic. During the cold (north) phase, subsurface conditions resemble a more clearly defined version of those described earlier in relation to the steady trade winds period. In the warm (south) phase, the mixed layer shoals and there is not a well-defined diurnal cycle of shear flow at our uppermost observation depth of 6.37 m. Negligible TIW modulation of diurnal SST amplitude is found, suggesting that similar wind-driven mixing continues above our observation depth, albeit with limited vertical penetration of the diurnal shear layers.
4. Concurrent with the descending diurnal shear layers observed during steady trade wind conditions, we observe marginal instability of an approximately 40 m thick layer below the mixed layer and above the thermocline. The strength of this layer appears to vary seasonally, tracking the shoaling thermocline and thinning substantially during the period of reduced wind stress in boreal winter. This property of marginal instability, along with the estimated turbulent dissipation rates, suggests a seasonality of deep cycle mixing that agrees with prior estimates of the seasonal cycle of mixing in the equatorial Atlantic [Foltz *et al.*, 2003; Hummels, 2012; Hummels *et al.*, 2013, 2014] and the equatorial Pacific [Smyth and Moum, 2013]. After the seasonal relaxation of local surface wind stress, we observe an approximately 2 week period where enhanced vertical shear during the south phase of a TIW contributes to the maintenance of a thick marginally unstable layer in the absence of diurnal shear variance.

These findings provide observational confirmation of prior diurnal cycle modeling work [Skielka *et al.*, 2011; Wade *et al.*, 2011] and indicate that many of the same dynamic processes that have been studied in the Pacific may also be active in the Atlantic [Gregg *et al.*, 1985; Moum and Caldwell, 1985; Peters *et al.*, 1994; Sun *et al.*, 1998]. In particular, observations of diurnal shear layers descending into the marginally unstable undercurrent layer suggests that we see both a mechanism for the initiation of deep-cycle turbulence [Smyth *et al.*, 2013; Pham *et al.*, 2013], as well as the resulting footprint on the flow stability [Smyth and Moum, 2013]. The regular occurrence of descending diurnal shear layers throughout the 2.5 months of observations during steady trade wind conditions can also be considered as evidence for the suggested role of diurnal shear in initiating deep-cycle turbulence, a finding enabled by the unique long moored-ADCP record of near-surface currents we utilize here. Currently, the limited dissipation measurements in the central equatorial Atlantic have been inconclusive in characterizing the diurnal cycle of turbulence [Crawford and Osborn, 1979; Hummels, 2012; Hummels *et al.*, 2013, 2014]. However, our findings suggest that future measurements are warranted, and will provide a useful point of comparison and contrast with the existing literature from the Pacific.

Appendix A : Uncertainty in dSSTa

The good agreement between complex demodulated dSSTa and estimates derived from direct differencing of daily maxima and minima gives us a basic level of confidence in our approach of estimating dSSTa (section 3). Additional uncertainty estimates for the complex demodulated dSSTa can be formulated using Monte Carlo simulation. Complex demodulation was performed on repeated realizations of a synthetic signal, consisting of a diurnal oscillation of known amplitude plus Gaussian white noise with variance scaled to match the SST observations in a spectral window surrounding the diurnal frequency, excluding the diurnal peak [Pawlowicz *et al.*, 2002]. Standard errors are then estimated from the synthetic signals using the median absolute deviation, and are found to be a very weak function of amplitude. Hence, 95% confidence intervals on the complex demodulated diurnal SST amplitude are well approximated by a constant value, $\pm 0.031^\circ\text{C}$ for daily averaged estimates.

Appendix B : Errors in S_{red}^2

We consider errors in calculated values of S_{red}^2 arising from three sources: instrumental noise, the approximately 12.5 km horizontal separation between the deep ADCP mooring and the surface mooring on which temperature and salinity observations were made (section 2.2), and the vertical resolution of the observations.

B1. Instrumental Noise and Horizontal Separation

We assume that instrumental noise, and horizontal separation, can be treated as additive errors, such that $u_{obs} = u + \epsilon_u$, and $\rho_{obs} = \rho + \epsilon_\rho$.

Above 35 m, ϵ_u will result solely from instrumental error, which can be calculated using the published single-ping variance for the 600 kHz ADCP configured as deployed, giving $\epsilon_u = 8.7 \times 10^{-3} \text{ m s}^{-1}$ for ensemble averaged values. Below 35 m, ϵ_u will consist of both instrumental error and errors due to the approximately 12.5 km horizontal separation between the ADCP mooring and the surface mooring. The upward and downward-facing ADCPs have overlapping velocity observations at 35 m depth, and hence we can treat the RMS difference between these observations as representing error due to horizontal separation. Using this approach we find $\epsilon_u = 0.17 \text{ m s}^{-1}$. This value is also roughly consistent with alternate estimates derived by adopting Taylor's frozen turbulence hypothesis, equating temporal shifts with horizontal separation [see also Smyth and Moum, 2013, Supplementary Information].

The value of ϵ_ρ is calculated in a similar manner, using the ATLAS mooring temperature (salinity) sensor accuracy of $\pm 0.02^\circ\text{C}$ (± 0.02) [Freitag et al., 2005]. A linearized equation of state is used to give $\epsilon_\rho = 6.4 \times 10^{-3} \text{ kg m}^{-3}$ for ensemble hourly averages of 10 min data. This estimate is likely conservative, as it applies post-deployment sensor drift errors to the entire observational period [Freitag et al., 2005].

The effect of these observational errors on finite difference calculations can be assessed using

$$\epsilon_z = \frac{\sqrt{2}\epsilon}{\Delta z} \quad (\text{B1})$$

where we have assumed that errors are uncorrelated across depth bins. Application of B1 gives, $\epsilon_{u_z} = 2.3 \times 10^{-3} \text{ s}^{-1}$ ($\epsilon_{u_z} = 2.4 \times 10^{-2} \text{ s}^{-1}$), and $\epsilon_{N^2} = 1.7 \times 10^{-5} \text{ s}^{-2}$ ($\epsilon_{N^2} = 8.7 \times 10^{-6} \text{ s}^{-2}$) for hourly estimates above (below) 35 m.

These values are then used in the propagation of errors formula to give an estimate of the total error in an hourly calculated value of S_{red}^2 ,

$$\epsilon_{S_{red}^2} \approx \left[\left(\frac{\partial S_{red}^2}{\partial u_z} \epsilon_{u_z} \right)^2 + \left(\frac{\partial S_{red}^2}{\partial N^2} \epsilon_{N^2} \right)^2 \right]^{\frac{1}{2}} = 2 \left[u_z^2 \epsilon_{u_z}^2 + 4 \epsilon_{N^2}^2 \right]^{\frac{1}{2}} \quad (\text{B2})$$

where we have ignored a term involving the covariance between u_z and N^2 as it is found to be small compared to other terms. Using average values for u_z , we find errors in hourly calculated values of S_{red}^2 on the order of $1.1 \times 10^{-4} \text{ s}^{-2}$ ($8.9 \times 10^{-4} \text{ s}^{-2}$) above (below) 35 m depth. Uncertainties of this magnitude do not alter the interpretation of the statistics used in this analysis.

B2. Vertical Resolution

The effect of the vertical separation between instruments, in particular the coarse resolution of temperature and salinity, cannot be assessed directly using our data. However, previous work suggests that the effect of lowering vertical resolution on the calculation of Richardson number is to alter the skewness of the distribution, rather than fundamentally altering the basic shape of the probability distribution [Smyth and Moum, 2013]. We thus expect that the coarse mooring vertical resolution will shift the calculated S_{red}^2 toward more stable values, without qualitatively changing our major findings.

It is possible to estimate the effect of vertical resolution on the calculation of N^2 in the upper 100 m using 38 available CTD casts from the World Ocean Database [Boyer et al., 2013] within $\pm 1^\circ$ of latitude and longitude of the mooring that have vertical resolution of at least 1 m and the first observation above 40 m depth. To accomplish this, estimates of N^2 are calculated for each CTD profile using the full resolution of the profile, which we treat as representing the true N^2 . CTD observations of temperature and salinity are then

decimated to observation depths consistent with the mooring sampling scheme, and new N_{dec}^2 are calculated. Differences between these values can be considered as errors due to the vertical sampling scheme employed by the PIRATA mooring.

Values of N^2 and N_{dec}^2 calculated in this manner are well correlated above 30 m ($r = 0.78$), and over the upper 100 m ($r = 0.62$). We use robust linear regression of the form $N_{dec}^2 = \hat{\beta}N^2 + \epsilon$, where ϵ are the errors in N_{dec}^2 that we seek to minimize. Applying this to the CTD data between the surface and 100 m depth gives, $\hat{\beta} = 0.84$, suggesting a low bias in N_{dec}^2 . We reran the analysis of this study after adjusting the observed values of N^2 to account for this bias and found that the major results are robust to this change. Further, alternate values of $\hat{\beta}$ ranging from 0.5 to 1.5 were tested, and the results were found to be qualitatively robust to these adjustments.

Acknowledgments

The authors would like to thank Eric Kunze and Ren-Chieh Lien for helpful discussions of this work, as well as Bill Smyth and an anonymous reviewer for their comments. We also thank Paul Freitag and the TAO project office of PMEL for their ongoing work on the PIRATA array. Patricia Plimpton completed the initial processing of the near-surface ADCP data. This publication is partially funded by the Joint Institute for the Study of the Atmosphere and Ocean (JISAO) under NOAA Cooperative Agreement NA10OAR4320148, JISAO contribution 2402, and PMEL contribution 4244. PIRATA mooring data are available at <http://www.pmel.noaa.gov/tao/>. PIRATA ADCP data are available from paul.freitag@noaa.gov. OLR and SST data are available from <http://www.esrl.noaa.gov/psd/data/>. Scatterometer Climatology of Ocean Winds from <http://cioss.coas.oregonstate.edu/scow/>, and World Ocean Database CTD data from http://www.nodc.noaa.gov/OC5/WOD/pr_wod.html.

References

- Bernie, D. J., E. Guilyardi, G. Madec, J. M. Slingo, and S. J. Woolnough (2007), Impact of resolving the diurnal cycle in an ocean-atmosphere GCM. Part 1: A diurnally forced OGCM, *Clim. Dyn.*, 29(6), 575–590, doi:10.1007/s00382-007-0249-6.
- Bernie, D. J., E. Guilyardi, G. Madec, J. M. Slingo, S. J. Woolnough, and J. Cole (2008), Impact of resolving the diurnal cycle in an ocean-atmosphere GCM. Part 2: A diurnally coupled CGCM, *Clim. Dyn.*, 31(7–8), 909–925, doi:10.1007/s00382-008-0429-z.
- Bloomfield, P. (1976), *Fourier Decomposition of Time Series: An Introduction*, John Wiley, N. Y.
- Bond, N. A., and M. J. McPhaden (1995), An indirect estimate of the diurnal cycle in upper ocean turbulent heat fluxes at the equator, 140W, *J. Geophys. Res.*, 100(C9), 18,369–18,378, doi:10.1029/95JC01592.
- Bourlès, B., et al. (2008), The PIRATA program: History, accomplishments, and future directions, *Bull. Am. Meteorol. Soc.*, 89(8), 1111–1125, doi:10.1175/2008BAMS2462.1.
- Boyer, T. P., et al. (2013), World Ocean Database 2013, *NOAA Atlas NESDIS 72*, Natl. Ocean. Atmos. Admin., Silver Spring, Md.
- Brainerd, K. E., and M. C. Gregg (1993), Diurnal restratification and turbulence in the oceanic surface mixed layer: 1. Observations, *J. Geophys. Res.*, 98(C12), 22,645–22,656, doi:10.1029/93JC02297.
- Brainerd, K. E., and M. C. Gregg (1995), Surface mixed and mixing layer depths, *Deep Sea Res., Part I*, 42(9), 1521–1543, doi:10.1016/0967-0637(95)00068-H.
- Chelton, D., and S.-P. Xie (2010), Coupled ocean-atmosphere interaction at oceanic mesoscales, *Oceanography*, 23(4), 52–69, doi:10.5670/oceanog.2010.05.
- Chen, S. S., and R. A. Houze (1997), Diurnal variation and life-cycle of deep convective systems over the tropical pacific warm pool, *Q. J. R. Meteorol. Soc.*, 123(538), 357–388, doi:10.1002/qj.49712353806.
- Clayson, C. A., and A. Chen (2002), Sensitivity of a coupled single-column model in the tropics to treatment of the interfacial parameterizations, *J. Clim.*, 15(14), 1805–1831, doi:10.1175/1520-0442(2002)015<1805:SOACSC>2.0.CO;2.
- Clayson, C. A., and J. A. Curry (1996), Determination of surface turbulent fluxes for the tropical ocean-global atmosphere coupled ocean-atmosphere response experiment: Comparison of satellite retrievals and in situ measurements, *J. Geophys. Res.*, 101(C12), 28,515–28,528, doi:10.1029/96JC02022.
- Clayson, C. A., and D. Weitlich (2007), Variability of tropical diurnal sea surface temperature, *J. Clim.*, 20(2), 334–352, doi:10.1175/JCLI3999.1.
- Crawford, W. R., and T. R. Osborn (1979), Microstructure measurements in the Atlantic equatorial undercurrent during GATE, *Deep Sea Res., Part A*, 26, suppl. 2, 285–308.
- Cronin, M. F., and W. S. Kessler (2002), Seasonal and interannual modulation of mixed layer variability at 0°, 110°W, *Deep Sea Res., Part I*, 49(1), 1–17, doi:10.1016/S0967-0637(01)00043-7.
- Cronin, M. F., and W. S. Kessler (2009), Near-surface shear flow in the tropical pacific cold tongue front, *J. Phys. Oceanogr.*, 39(5), 1200–1215, doi:10.1175/2008JPO4064.1.
- Cronin, M. F., and M. J. McPhaden (1999), Diurnal cycle of rainfall and surface salinity in the Western Pacific Warm Pool, *Geophys. Res. Lett.*, 26(23), 3465–3468, doi:10.1029/1999GL010504.
- Dai, A., and K. E. Trenberth (2004), The diurnal cycle and its depiction in the community climate system model, *J. Clim.*, 17(5), 930–951, doi:10.1175/1520-0442(2004)017<0930:TDCAD>2.0.CO;2.
- Danabasoglu, G., W. G. Large, J. J. Tribbia, P. R. Gent, B. P. Briegleb, and J. C. McWilliams (2006), Diurnal coupling in the tropical oceans of CCSM3, *J. Clim.*, 19(11), 2347–2365, doi:10.1175/JCLI3739.1.
- Donlon, C. J., P. J. Minnett, C. Gentemann, T. J. Nightingale, I. J. Barton, B. Ward, and M. J. Murray (2002), Toward improved validation of satellite sea surface skin temperature measurements for climate research, *J. Clim.*, 15(4), 353–369, doi:10.1175/1520-0442(2002)015<0353:TIVOSS>2.0.CO;2.
- Drushka, K., S. T. Gille, and J. Sprintall (2014), The diurnal salinity cycle in the tropics, *J. Geophys. Res. Oceans*, 119, 5874–5890, doi:10.1002/2014JC009924.
- Efron, B., and R. Tibshirani (1993), An introduction to the bootstrap, in *Monographs on Statistics and Applied Probability*, vol. 57, Chapman and Hall, N. Y.
- Fairall, C. W., E. F. Bradley, J. E. Hare, A. A. Grachev, and J. B. Edson (2003), Bulk parameterization of air-sea fluxes: Updates and verification for the COARE algorithm, *J. Clim.*, 16(4), 571–591, doi:10.1175/1520-0442(2003)016<0571:BPOASF>2.0.CO;2.
- Flato, G., et al. (2013), 2013: Evaluation of climate models, in *Climate Change 2013: The Physical Science Basis. Contribution of Working Group I to the Fifth Assessment Report of the Intergovernmental Panel on Climate Change*, edited by T. F. Stocker et al., Cambridge Univ. Press, Cambridge, U. K.
- Foltz, G. R., and M. J. McPhaden (2010), Abrupt equatorial wave-induced cooling of the Atlantic cold tongue in 2009, *Geophys. Res. Lett.*, 37, L24605, doi:10.1029/2010GL045522.
- Foltz, G. R., S. A. Grodsky, J. A. Carton, and M. J. McPhaden (2003), Seasonal mixed layer heat budget of the tropical Atlantic Ocean, *J. Geophys. Res.*, 108(C5), 3146, doi:10.1029/2002JC001584.
- Foltz, G. R., M. J. McPhaden, and R. Lumpkin (2012), A strong Atlantic meridional mode event in 2009: The role of mixed layer dynamics, *J. Clim.*, 25(1), 363–380, doi:10.1175/JCLI-D-11-00150.1.

- Freitag, H. P., T. A. Sawatzky, K. B. Ronnholm, and M. J. McPhaden (2005), Calibration procedures and instrumental accuracy estimates of next generation ATLAS water temperature and pressure measurements, *NOAA Tech. Memo. OAR PMEL-128, NTIS: PB2008-101764*, NOAA/Pacific Marine Environmental Laboratory, Seattle, Wash.
- Gregg, M. C., H. Peters, J. C. Wesson, N. S. Oakey, and T. J. Shay (1985), Intensive measurements of turbulence and shear in the equatorial undercurrent, *Nature*, *318*(6042), 140–144, doi:10.1038/318140a0.
- Grodsky, S. A., J. A. Carton, C. Provost, J. Servain, J. A. Lorenzetti, and M. J. McPhaden (2005), Tropical instability waves at 0°N, 23°W in the Atlantic: A case study using pilot research moored array in the tropical Atlantic (PIRATA) mooring data, *J. Geophys. Res.*, *110*, C08010, doi:10.1029/2005JC002941.
- Halpern, D., and R. K. Reed (1976), Heat budget of the upper ocean under light winds, *J. Phys. Oceanogr.*, *6*(6), 972–975, doi:10.1175/1520-0485(1976)006<0972:HBOTUO>2.0.CO;2.
- Hazel, P. (1972), Numerical studies of the stability of inviscid stratified shear flows, *J. Fluid Mech.*, *51*(1), 39–61, doi:10.1017/S0022112072001065.
- Hummels, R. (2012), On the variability of turbulent mixing within the upper layers of the Atlantic cold tongue region, PhD thesis, Universitätsbibliothek Kiel, Kiel, Germany.
- Hummels, R., M. Dengler, and B. Bourlès (2013), Seasonal and regional variability of upper ocean diapycnal heat flux in the Atlantic cold tongue, *Prog. Oceanogr.*, *111*, 52–74, doi:10.1016/j.pocean.2012.11.001.
- Hummels, R., M. Dengler, P. Brandt, and M. Schlundt (2014), Diapycnal heat flux and mixed layer heat budget within the Atlantic cold tongue, *Clim. Dyn.*, *43*, 3179–3199, doi:10.1007/s00382-014-2339-6.
- Inoue, R., R.-C. Lien, and J. N. Moum (2012), Modulation of equatorial turbulence by a tropical instability wave, *J. Geophys. Res.*, *117*, C10009, doi:10.1029/2011JC007767.
- Jochum, M., P. Malanotte-Rizzoli, and A. Busalacchi (2004), Tropical instability waves in the Atlantic Ocean, *Ocean Modell.*, *7*(1–2), 145–163, doi:10.1016/S1463-5003(03)00042-8.
- Kunze, E., A. J. Williams, and M. G. Briscoe (1990), Observations of shear and vertical stability from a neutrally buoyant float, *J. Geophys. Res.*, *95*(C10), 18,127–18,142, doi:10.1029/JC095C10p18127.
- Legeckis, R. (1977), Long waves in the eastern equatorial Pacific Ocean: A view from a geostationary satellite, *Science*, *197*(4309), 1179–1181, doi:10.1126/science.197.4309.1179.
- Liebmann, B., and C. A. Smith (1996), Description of a complete (interpolated) outgoing longwave radiation dataset, *Bull. Am. Meteorol. Soc.*, *77*(6), 1275–1277.
- Lien, R.-C., D. R. Caldwell, M. C. Gregg, and J. N. Moum (1995), Turbulence variability at the equator in the central Pacific at the beginning of the 1991–1993 El Niño, *J. Geophys. Res.*, *100*(C4), 6881–6898.
- Lien, R.-C., E. A. D'Asaro, and C. E. Menkes (2008), Modulation of equatorial turbulence by tropical instability waves, *Geophys. Res. Lett.*, *35*, L24607, doi:10.1029/2008GL035860.
- Maur, M. F. (1855), *The Physical Geography of the Sea, and Its Meteorology*, Sampson Low, Son & Marston, London, U. K.
- McPhaden, M. J. (1993), Trade wind fetch-related variations in equatorial undercurrent depth, speed, and transport, *J. Geophys. Res.*, *98*(C2), 2555–2559, doi:10.1029/92JC02683.
- Moum, J. N., and D. R. Caldwell (1985), Local influences on shear-flow turbulence in the equatorial ocean, *Science*, *230*(4723), 315–316, doi:10.1126/science.230.4723.315.
- Moum, J. N., R.-C. Lien, A. Perlin, J. D. Nash, M. C. Gregg, and P. J. Wiles (2009), Sea surface cooling at the equator by subsurface mixing in tropical instability waves, *Nat. Geosci.*, *2*(11), 761–765, doi:10.1038/ngeo657.
- Moum, J. N., A. Perlin, J. D. Nash, and M. J. McPhaden (2013), Seasonal sea surface cooling in the equatorial Pacific cold tongue controlled by ocean mixing, *Nature*, *500*(7460), 64–67, doi:10.1038/nature12363.
- Pawlowicz, R., B. Beardsley, and S. Lentz (2002), Classical tidal harmonic analysis including error estimates in MATLAB using T_TIDE, *Comput. Geosci.*, *28*(8), 929–937, doi:10.1016/S0098-3004(02)00013-4.
- Peters, H., and M. C. Gregg (1988), *Some Dynamical and Statistical Properties of Equatorial Turbulence*, Elsevier Oceanogr. Ser., vol. 46, pp. 185–200, Elsevier, Amsterdam.
- Peters, H., M. C. Gregg, and T. B. Sanford (1994), The diurnal cycle of the upper equatorial ocean: Turbulence, fine-scale shear, and mean shear, *J. Geophys. Res.*, *99*(C4), 7707–7723, doi:10.1029/93JC03506.
- Peters, H., M. C. Gregg, and T. B. Sanford (1995), On the parameterization of equatorial turbulence: Effect of fine-scale variations below the range of the diurnal cycle, *J. Geophys. Res.*, *100*(C9), 18,333–18,348, doi:10.1029/95JC01513.
- Pham, H. T., S. Sarkar, and K. B. Winters (2013), Large-eddy simulation of deep-cycle turbulence in an equatorial undercurrent model, *J. Phys. Oceanogr.*, *43*(11), 2490–2502, doi:10.1175/JPO-D-13-016.1.
- Polzin, K. (1996), Statistics of the Richardson number: Mixing models and finestructure, *J. Phys. Oceanogr.*, *26*(8), 1409–1425, doi:10.1175/1520-0485(1996)026<1409:SOTRNM>2.0.CO;2.
- Price, J. F., R. A. Weller, and R. Pinkel (1986), Diurnal cycling: Observations and models of the upper ocean response to diurnal heating, cooling, and wind mixing, *J. Geophys. Res.*, *91*(C7), 8411–8427, doi:10.1029/JC091C07p08411.
- Reynolds, R. W., N. A. Rayner, T. M. Smith, D. C. Stokes, and W. Wang (2002), An improved in situ and satellite SST analysis for climate, *J. Clim.*, *15*(13), 1609–1625, doi:10.1175/1520-0442(2002)015<1609:AISAS>2.0.CO;2.
- Risien, C. M., and D. B. Chelton (2008), A global climatology of surface wind and wind stress fields from eight years of QuikSCAT scatterometer data, *J. Phys. Oceanogr.*, *38*(11), 2379–2413, doi:10.1175/2008JPO3881.1.
- Santiago-Mandujano, F., and E. Firing (1990), Mixed-layer shear generated by wind stress in the central equatorial Pacific, *J. Phys. Oceanogr.*, *20*(10), 1576–1582, doi:10.1175/1520-0485(1990)020<1576:MLSGWB>2.0.CO;2.
- Servain, J. (1991), Simple climatic indices for the tropical Atlantic Ocean and some applications, *J. Geophys. Res.*, *96*(C8), 15,137–15,146, doi:10.1029/91JC01046.
- Servain, J., A. J. Busalacchi, M. J. McPhaden, A. D. Moura, G. Reverdin, M. Vianna, and S. E. Zebiak (1998), A pilot research moored array in the tropical Atlantic (PIRATA), *Bull. Am. Meteorol. Soc.*, *79*(10), 2019–2031, doi:10.1175/1520-0477(1998)079<2019:APRMAI>2.0.CO;2.
- Shinoda, T. (2005), Impact of the diurnal cycle of solar radiation on intraseasonal SST variability in the Western Equatorial Pacific, *J. Clim.*, *18*(14), 2628–2636, doi:10.1175/JCLI3432.1.
- Sillmann, J., V. V. Kharin, X. Zhang, F. W. Zwiers, and D. Bronaugh (2013), Climate extremes indices in the CMIP5 multimodel ensemble: Part 1. Model evaluation in the present climate: Climate extremes indices in CMIP5, *J. Geophys. Res. Atmos.*, *118*, 1716–1733, doi:10.1002/jgrd.50203.
- Skielka, U. T., J. Soares, A. P. Oliveira, and J. Servain (2011), Diagnostic of the diurnal cycle of turbulence of the Equatorial Atlantic Ocean upper boundary layer, *Nat. Sci.*, *3*(6), 444–455, doi:10.4236/ns.2011.36061.

- Smyth, W. D., and J. N. Moum (2013), Marginal instability and deep cycle turbulence in the eastern equatorial Pacific Ocean, *Geophys. Res. Lett.*, *40*, 6181–6185, doi:10.1002/2013GL058403.
- Smyth, W. D., J. N. Moum, L. Li, and S. A. Thorpe (2013), Diurnal shear instability, the descent of the surface shear layer, and the deep cycle of equatorial turbulence, *J. Phys. Oceanogr.*, *43*(11), 2432–2455, doi:10.1175/JPO-D-13-089.1.
- Smyth, W. H. (1854), *The Mediterranean: A Memoir, Physical, Historical and Nautical*, J. W. Parker and Son, London, U. K.
- Stommel, H., K. Saunders, W. Simmons, and J. Cooper (1969), Observations of the diurnal thermocline, *Deep Sea Res. Oceanogr. Abstr.*, *16*, 269–284.
- Stuart-Menteth, A. C., I. S. Robinson, and P. G. Challenor (2003), A global study of diurnal warming using satellite-derived sea surface temperature, *J. Geophys. Res.*, *108*(C5), 3155, doi:10.1029/2002JC001534.
- Stull, R. B. (1950), *An Introduction to Boundary Layer Meteorology*, Kluwer Acad., Dordrecht, Netherlands.
- Sun, C., W. D. Smyth, and J. N. Moum (1998), Dynamic instability of stratified shear flow in the upper equatorial Pacific, *J. Geophys. Res.*, *103*(C5), 10,323–10,337, doi:10.1029/98JC00191.
- Thorpe, S. A., and Z. Liu (2009), Marginal instability?, *J. Phys. Oceanogr.*, *39*(9), 2373–2381, doi:10.1175/2009JPO4153.1.
- Wade, M., G. Caniaux, Y. duPenhoat, M. Dengler, H. Giordani, and R. Hummels (2011), A one-dimensional modeling study of the diurnal cycle in the equatorial Atlantic at the PIRATA buoys during the EGEE-3 campaign, *Ocean Dyn.*, *61*(1), 1–20, doi:10.1007/s10236-010-0337-8.
- Waliser, D. E., and C. Gautier (1993), A satellite-derived climatology of the ITCZ, *J. Clim.*, *6*(11), 2162–2174, doi:10.1175/1520-0442(1993)006<2162:ASDCOT>2.0.CO;2.
- Ward, B. (2006), Near-surface ocean temperature, *J. Geophys. Res.*, *111*, C02005, doi:10.1029/2004JC002689.
- Weisberg, R. H., and T. J. Weingartner (1988), Instability waves in the equatorial Atlantic ocean, *J. Phys. Oceanogr.*, *18*(11), 1641–1657, doi:10.1175/1520-0485(1988)018<1641:WITEA>2.0.CO;2.
- Wenegrat, J. O., M. J. McPhaden, and R.-C. Lien (2014), Wind stress and near-surface shear in the equatorial Atlantic Ocean, *Geophys. Res. Lett.*, *41*, 1226–1231, doi:10.1002/2013GL059149.
- Wilcox, R. R. (2010), *Fundamentals of Modern Statistical Methods: Substantially Improving Power and Accuracy*, 2nd ed., Springer, N. Y.
- Woolnough, S. J., F. Vitart, and M. A. Balmaseda (2007), The role of the ocean in the Madden-Julian oscillation: Implications for MJO prediction, *Q. J. R. Meteorol. Soc.*, *133*(622), 117–128, doi:10.1002/qj.4.
- Xie, S.-P., and J. A. Carton (2004), *Tropical Atlantic Variability: Patterns, Mechanisms, and Impacts*, *Geophys. Monogr. Ser.*, vol. 147, edited by C. Wang, S.-P. Xie, and J. A. Carton, pp. 121–142, AGU, Washington, D. C.
- Zebiak, S. E. (1993), Air-Sea interaction in the equatorial Atlantic region, *J. Clim.*, *6*(8), 1567–1586, doi:10.1175/1520-0442(1993)006<1567:AIITEA>2.0.CO;2.